Journal of Materials Chemistry A

ROYAL SOCIETY OF CHEMISTRY

PAPER

View Article Online
View Journal

Cite this: DOI: 10.1039/d6ta00313c

Pulse-mediated refaceting of copper. Influence on 5-hydroxymethylfurfural electrocatalysis

Vicente Pascual-Llorens, [a] Lorena Chico-Mesa, [b] Michael Musi, [c] Rosa M. Arán-Ais *[b] and Paula Sebastián-Pascual *[a]

This work evaluates the impact of the reduction potential (E_R) on the pulse-mediated formation of high-index facet structures on Cu(111) and copper polycrystalline electrode in sodium chloride (NaCl) electrolyte. Cyclic voltammetry (CV), electron backscatter diffraction (EBSD), and scanning electron microscopy (SEM) were combined to correlate grain orientation and surface morphology changes with experimental conditions that drive shape formation. Furthermore, we have performed a comprehensive voltammetric analysis across a broad range of stepped single crystal electrodes, demonstrating that blank CVs of the Cu | 0.1 M NaCl interface effectively decouple terrace and step contributions on copper. Our study revealed that while chloride tends to induce structures comprising (100) terraces and (111) or (110) steps under oxidation–reduction potential pulse conditions, the deposition rate, determined by the E_R, controls the length of the generated (100) terraces and defect density. The oxidation and reduction of 5-hydroxymethylfurfural (HMF) were investigated as model structure-sensitive reactions to probe how variations in the terrace-to-defect ratio affect catalytic behaviour. Low-coordinated sites promote oxidation of HMF, whereas (100) terraces adjacent to steps decrease the onset potential for HMF reduction. By identifying the active surface facets, this work demonstrates that surface structure engineering is a powerful approach to advance electrocatalysis on copper.

Received 12th January 2026
Accepted 8th April 2026

DOI: 10.1039/d6ta00313c

rsc.li/materials-a

Introduction

The use of oxidation and reduction potential (E_R) pulses to tune the surface structure of copper has gained increasing attention over the past decade, particularly as a strategy to exploit its electrocatalytic performance.[1–4] The potential pulse technique, also known as the square wave potential (SWP) method, alternates the application of an anodic potential, where copper dissolves, and a cathodic potential, where the dissolved copper is redeposited.[5,6] Pulse durations typically range from seconds to several milliseconds, corresponding to frequencies between 1 and 100 Hz.[1,3,7] These fast potential perturbations cause surface restructuring, the appearance of structural motifs,[3,8] and changes in the oxidation states of copper,[1,3,8] all of which alter the catalytic performance of the pristine surface. This strategy has been employed, for instance, to tune the selectivity of a Cu(100) single facet during electrochemical carbon dioxide (CO_2) reduction, favouring the formation of ethanol over ethylene.[1,3] Yet, there is a lack of systematic studies addressing how the conditions of the potential-pulse method, such as time, applied potential limits, and deposition rate, affect the surface refaceting mechanism on copper.

Notably, the use of the SWP method for surface refaceting of other metals, such as platinum and palladium, was already established in the late 1980s.[6] Arvia *et al.* demonstrated that potential pulses could be used to induce the formation of short and long-range (100) terrace domains on polycrystalline platinum.[9,10] Later in the 2000s, Sun and coworkers extended the use of the SWP technique for the electrodeposition of platinum (Pt) and palladium (Pd) shaped nanoparticles with high index facets, focusing on the effect of both time and applied potential limits in nanoparticle shape evolution.[5,7,11] They proved that the number of steps and kinks could be finely tailored on Pt by varying either the E_R limit, which controls the deposition rate, or by changing the oxidation potential limit, which affects the surface etching rate.[7] In another study, the same authors observed a shape transition from tetrahexahedral Pt nanoparticles with high-index (n10) facets to cubic particles with increased time periods of applied potential pulses. These results illustrated that the growth of low-index (100) facets takes more time on pulse-mediated electrodeposition of Pt.[12] Inspired by these studies, our group has recently reported the surface refaceting of Cu(111) using the SWP method in sodium chloride (NaCl) electrolyte.[13] The application of pulses at very negative E_R or high deposition rates formed hexagonal pyramids

[a]Wallenberg Initiative Materials Science for Sustainability, Department of Chemistry, School of Engineering Science in Chemistry, Biochemistry and Health, KTH Royal Institute of Technology, Stockholm, Sweden. E-mail: paulasp@kth.se

[b]Instituto de Electroquímica, Universidad de Alicante, Apdo. 99, E-03080, Alicante, Spain. E-mail: rosa.aran@ua.es

[c]Unit of Hultgren Laboratory for Materials Characterisation, Department of Materials Science and Engineering, KTH Royal Institute of Technology, Stockholm, Sweden

resembling truncated tetrahexadral ($n10$) clusters,[14] growing on top of the (111) plane. At longer deposition times, the emergence of a few triangular pyramids accompanied by larger, irregular clusters was observed, indicating that pulse-mediated refaceting of copper is a dynamic process. These triangular pyramids resembled cubic particles intersected by a (111) plane, suggesting that the formation of low-index (100) sites requires a longer development time on copper.[12]

Previous studies on Pt have demonstrated that the pulsed-mediated formation of high and low index facets is potential-dependent and not only electrolyte-dependent.[7] Considering these insights on Pt, this work aims to investigate how the E_R limit affects the formation of (100) terrace domains of tuneable length during pulsed-mediated refaceting of copper in NaCl electrolyte. For the surface refaceting of copper, we have applied potential pulses at a frequency of 1 Hz, with E_R limits ranging from −1.30 V to −0.60 V *versus* the saturated calomel electrode (SCE). This potential range corresponds to the region where copper remains metallic in NaCl.[13] We started assessing the effect of the E_R limit on Cu(111), a mono-oriented electrode that we use as a model surface to evaluate the impact of the deposition rate on the formation of different morphologies with high-index facets. After tracking the potential dependent evolution of shaped structures on Cu(111), we modified a polycrystalline surface (Cu(poly)) containing different grains which orientations were determined using electron backscatter diffraction (EBSD).[15] With this analysis, we aim to assess how different substrate orientations influence copper refaceting[16] and test the usability of the potential-pulse method for tailoring the crystallographic domains of copper surfaces with variable structural complexity.

Knowing which geometric sites appear when copper is electrochemically refaceted is essential for linking surface structure to electrocatalytic behaviour. To date, there is a lack of studies assessing electrochemical methods that effectively distinguish terraces from step sites on copper. It was previously proposed that NaCl could be used not only to modify copper with pulses but also to electrochemically characterise copper's surface using cyclic voltammetry (CV).[13] Hori and coworkers indeed used electrolytes containing NaCl to characterise silver single facets for CO_2 reduction.[17] As with silver, chloride-specific adsorption is highly structure-sensitive on copper.[18,19] It provides voltammetric features for the (100) basal plane and for the (310) facet (a stepped surface with three-row (100) terraces and monoatomic (110) steps), which appear considerably separated in the electrode's CV.[13] These results suggested that NaCl could be used to identify both (100) terrace domains and step sites. To provide further support, this study conducts a comprehensive analysis of blank CVs on a broad range of single crystal surfaces with different indexes. Stepped surfaces, composed of terrace domains separated by monoatomic steps, are typically considered model electrodes to investigate how defects and low-coordinated sites influence the catalytic behaviour in nanostructured catalysts. This work focuses on assessing the electrochemical response of electrodes from the $[01\bar{1}]$ and $[\bar{1}00]$ crystallographic zones, specifically on Cu(S)$[n(100) \times (111)]$ and Cu(S)$[n(100) \times (110)]$ stepped surfaces. Our aim is to develop an electrochemical tool that can unambiguously distinguish between terrace and step contributions on all copper surfaces, regardless of how they have been prepared.

Although most studies using potential pulses aimed to tailor the copper catalyst structure to improve the electrochemical CO_2 reduction,[1,3,4,8] the catalytic versatility of copper goes beyond this reaction. In recent years, copper has also demonstrated promising performance in emerging reactions, such as partial oxidation[20] and the hydrogenation[21,22] of bio-based aldehydes, which occur at remarkably low onset potentials. In this work, the electrochemical behaviour of refaceted copper surfaces toward the oxidation and reduction of 5-hydroxymethyl furfural (HMF), a bio-based platform molecule derived from cellulose dehydration,[23] was also investigated. Particular attention was given to assessing how variations in the terrace-to-step or defect ratio on refaceted copper influence the onset potential for HMF reduction, as well as the catalytic activity reached during HMF oxidation.

Experimental

Electrochemical experiments were carried out in a classical three-electrode cell configuration at ambient temperature, employing two different cells: (1) a glass cell was used to record blank CVs in NaCl and perform lead underpotential deposition (Pb UPD) on copper; (2) the glass cell was replaced by a perfluoroalkoxy alkane (PFA) cell when the measurements were carried out in sodium hydroxide (NaOH) solution as glassware dissolution in alkaline media may introduce contaminants on the copper surface.[24] A calomel reference electrode (SCE) was employed for the experiments conducted in NaCl-containing solutions, whereas a mercury oxide (Hg/HgO) reference electrode built in a Teflon outer body was used for experiments in NaOH. A high-area copper wire was used as a counter-electrode in all experiments except for those performed in alkaline media, for which a graphite rod was used instead as a counter-electrode. The employed working electrodes were Cu single crystal (Cu(hkl)) and Cu polycrystalline (Cu(poly)) disk electrodes with 99.999% purity and geometric area of 0.1963 cm^{-2}, purchased from MaTeck GmbH. All experiments were conducted with the working electrode in the meniscus configuration and under an argon atmosphere. Before each experiment, the working electrode surface was electropolished in a two-electrode cell containing a diluted solution of 70% phosphoric acid (prepared from an 85% phosphoric acid solution, purchased from VMR Chemicals, Prolabo®).[25] Subsequently, a constant potential difference (ΔE) of 2.0 V was applied between the Cu electrode (anode) and a copper wire (cathode) for 30 seconds. Finally, the electropolished surface was thoroughly rinsed with ultrapure water (Direct-Q Millipore, 18.2 MΩ cm) to remove any excess acid before being transferred to the electrochemical cell. All the electrochemical experiments were conducted using a SP-300 multipotentiostat (BioLogic).

Before the experiments, the glassware and the glass cells were kept overnight in a saturated solution of $KMnO_4$ (Sigma-Aldrich, Emplura®). Thereupon, the glassware was rinsed with a diluted solution of H_2O_2 (33%, VMR Chemicals,

Prolabo®) + H_2SO_4 (96%, Sigma-Aldrich, Suprapur®) and boiled three times in ultrapure water. The PFA cell was cleaned in a piranha solution prepared with H_2O_2 and H_2SO_4 in the volume ratio of 50 : 50 and left in the solution overnight. Before conducting an experiment, the PFA cell was rinsed several times with ultrapure water to remove traces of piranha.

To modify the Cu(111) and Cu(poly) electrodes, we applied potential pulses between a reduction limit (E_R) of −1.30 V to −0.60 V *vs.* SCE, and a constant anodic limit at 0.5 V *vs.* SCE with a frequency of 1 Hz. Pulsed deposition was carried out at two different times (150 s and 300 s) in 0.1 M NaCl (from Sigma-Aldrich Merck, 99.999%). The electrochemical surface characterisation of the single crystals and refaceted copper surfaces was performed in 0.1 M NaCl at 50 mV s^{-1}, and in the potential window between −1.20 V and −0.40 V *vs.* SCE, where no solvent reduction or surface oxidation occurs. Pb UPD CVs at 5 mV s^{-1} were conducted in 0.1 M $KClO_4$ (from Sigma-Aldrich-Merck, 99.999%) + 1 mM $HClO_4$ (Merck Suprapur®) + 2 mM NaCl + 2 mM $Pb(ClO_4)_2$ (Sigma-Aldrich Merck, 99.99%) solution. The electrochemical characterisation in NaCl electrolyte and Pb UPD CVs were plotted against the SCE electrode, for consistency with previous reports.[13,14,26] Both the electrochemical oxidation and reduction of HMF (From 99%, Sigma-Aldrich) were studied in a PFA cell, with a modified Cu electrode as the working electrode, a Hg/HgO reference electrode, and the graphite rod electrode (Redox.me) as the counter electrode. The solution was prepared using 50 mM of HMF and 50 mM $NaOH \cdot H_2O$ (99.99%, Sigma-Aldrich Merck, Suprapur®), and the pH was fixed slightly below 13 to minimise the chemical degradation of HMF.[27] Electrocatalytic measurements were done at a slower scan rate of 10 mV s^{-1}. Before carrying out the HMF oxidation and reduction, blank CVs at 50 mV s^{-1} in 0.05 M NaOH were performed on each modified electrode to ensure surface cleanliness. Potentials referenced with the Hg/HgO electrode were scaled to the reversible hydrogen electrode (RHE) to better compare our results with previous reports on the electrochemical response of copper in alkaline media.[24,28,29] The potential conversion to the RHE electrode was done following a previous report.[30] The calculation of the IR drop was performed manually in line with the instructions outlined elsewhere.[31] Accordingly, solution resistance, R, was measured using potentiostatic electrochemical impedance spectroscopy (PEIS) in the double layer region of the metal-electrolyte interface.

Field-emission scanning electron microscopy (FE-SEM) analysis was performed to address the topology of the chloride-modified electrodes. The FE-SEM used in this study was a Thermo Fisher Scientific Apreo 2 s LoVac SEM. EBSD technique was employed to elucidate the crystallographic orientation and grain structure on the surface of the Cu(poly) electrode. The EBSD measurements were conducted in a SEM JEOL-7800F equipped with a Bruker Quantax loEBSD system operating at an acceleration voltage of 15 kV. Several EBSD scans across the surface were carried out with a step size of 0.15 μm to determine the orientation of the individual grains. Post-processing of the EBSD data was performed with the Quantax EBSD software from Bruker. VESTA (Visualisation for Electronic and Structural Analysis) software was used to draw the shaped particles and represent the atomic distribution of different crystallographic orientations.

Results and discussion

Influence of reduction potential on Cu(111) refaceting

The initial analysis examined how the deposition rate affects the early stages of formation of shaped structures on Cu(111) using the SWP method, by applying E_R values between −1.30 V and −0.60 V *vs.* SCE for 150 s. The morphological evolution was subsequently examined by FE-SEM, and the corresponding results are summarised in Fig. 1 and S1. Fig. 1A shows that at the less negative reduction potential of $E_R = -0.60$ V the surface exhibits the formation of numerous nanometric clusters. The largest clusters have a hexagonal morphology, as depicted in Fig. 1B. Fig. 1C and D outcome that applying a more negative E_R of −1.00 V induces the formation of pyramidal clusters with a predominantly triangular morphology. Fig. 1E and S1A illustrate that if the reduction rate is further made more negative by applying $E_R = -1.30$ V, the surface exhibits hexagonal pyramids of varying sizes, ranging from several hundred nanometres to a few micrometres, consistent with previous findings.[13]

Fig. S1B and S1C includes the results for other E_R values within the potential region of −1.30 V and −0.60 V. At E_R = −1.10 V (Fig. S1B) both hexagonal and more triangular structures form on the modified Cu(111), evidencing a morphology transition occurring when E_R is progressively changed from −1.30 V to −1.00 V. When a less negative reduction potential of −0.90 V is applied (Fig. S1C), the lateral facets of the triangular pyramids begin to open, leading to the reappearance of more hexagonal shapes, thereby evolving to the morphology appearance obtained at $E_R = -0.60$ V.

To better illustrate the potential-dependent evolution of shaped structures, we included in Fig. 1F schematic representations of tetrahexahedral particles intersected by a (111) plane, representing the growth of (n10) structures on a (111) surface. (n10) structures, which correspond to Cu(S)[n(100)(110)] stepped structures, were previously observed when Cu was refaceted in presence of chloride anions.[13,14] Fig. 1F depicts (n10) tetrahexahedral particles with short terrace domains (with $n = 2$ and 3, like (210) and (310)), as well as a particle with longer terrace domains (with $n > 3$, like (510) and (710)), which progressively develop a triangular shape during epitaxial growth on a (111) plane. The simulated growth processes of (n10) structures and the corresponding SEM images at each E_R are closely similar, tentatively suggesting the following interpretation: high deposition rates in which negative E_R (−1.30 V) are applied preferentially induce the formation of highly undercoordinated (n10) structures. In contrast, moderate E_R (−1.00 V) favours the development of more triangular shapes, indicative of the presence of larger terrace (100) sites. When the deposition rate is too slow (E_R of −0.60 V), highly undercoordinated and nanometric structures are primarily promoted. The SI includes an analysis of the angles between the lateral sides in the shaped structures formed at different E_R (Fig. S1 and S2), which suggests that the pulsed deposition of (n10) with different (100) terrace length is

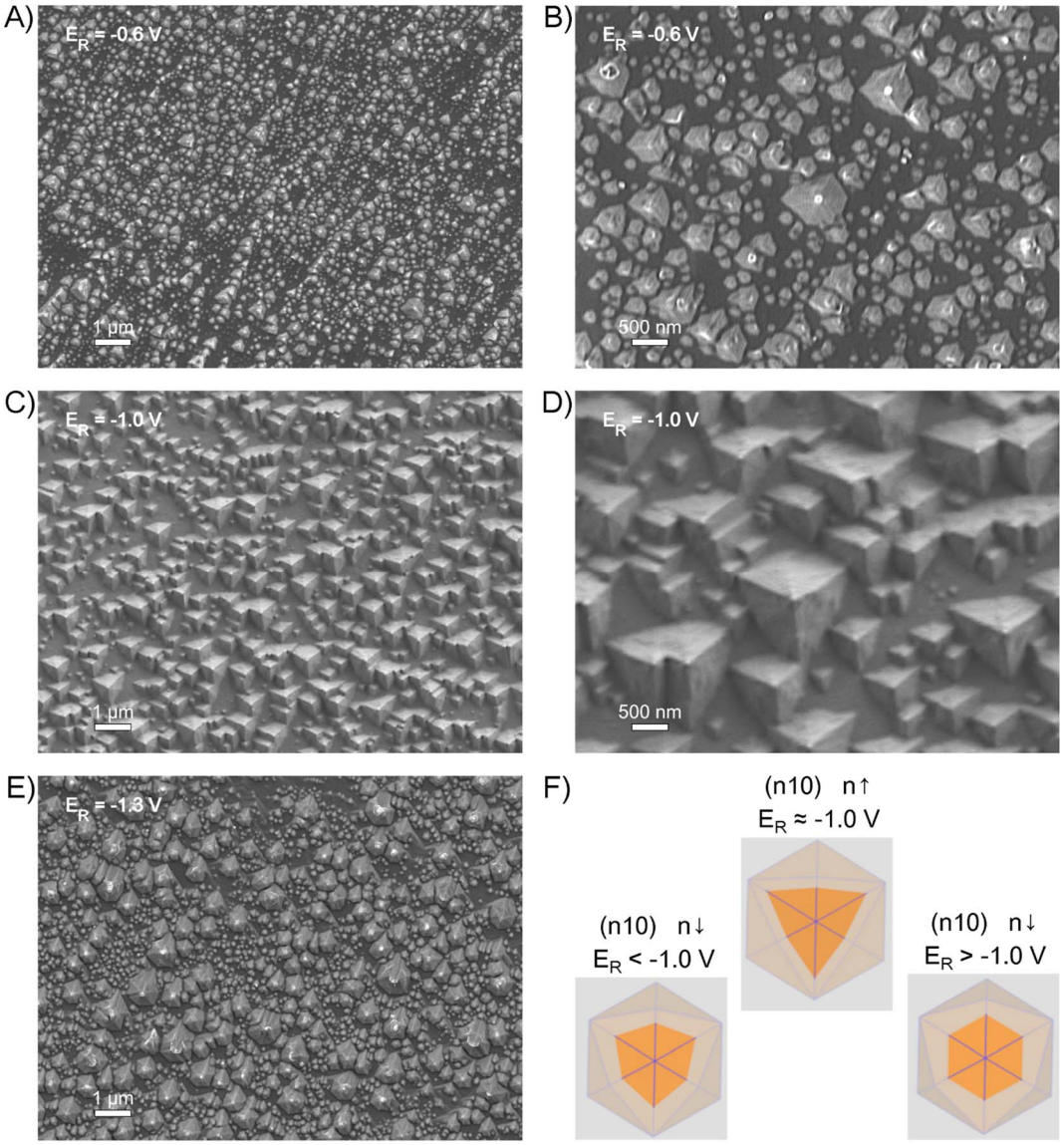

Fig. 1 SEM images of modified Cu(111) electrodes at different E_R values after 150 s. (A) and (B) $E_R = -0.60$ V *vs.* SCE at different magnifications. (C) and (D) $E_R = -1.00$ V *vs.* SCE at different magnifications. (E) $E_R = -1.30$ V *vs.* SCE. (F) Simulated structure morphologies for E_R more negative than −1.00 V; E_R around −1.00 V; and E_R less negative than −1.00 V.

potential-dependent. To further confirm that potential pulses in NaCl form structures with tuneable terrace-to-step ratio and address the contribution of each newly formed facet in the electrode surface, cyclic voltammetry technique was used to characterise refaceted Cu(111).

The site-specific adsorption of species has traditionally been investigated using cyclic voltammetry in various electrolytes. For instance, the hydrogen underpotential deposition (H-UPD) region serves as a fingerprint for Pt surfaces,[32] while OH adsorption[28] and Pb underpotential deposition (Pb UPD)[14,33] have been employed to characterise Cu surfaces, with the latter providing a more precise identification of Cu sites. For this reason, Pb UPD was initially employed to identify the different facets and their distribution resulting from the pulsed protocol applied to Cu(111) at various E_R (−1.30 V, −1.00 V, and −0.60 V).[26,33,34] To increase the intensity of voltammetric features of new electrochemically induced facets in relation to the (111) substrate contribution, the copper Cu(111) was refaceted for a more extended period of time by applying pulses during 300 s. Fig. S3A–E includes SEM images of the Cu(111) modified for 300 s, which display morphological structures essentially similar to those obtained for 150 s in Fig. 1, but bigger in size or more overlapped.[13] A complete description of the Pb UPD CVs is provided in the SI, and the corresponding results are shown in Fig. S3F. The considerable overlap between peaks in the Pb UPD CVs makes it difficult to distinguish step contributions from those of the (100) terraces in (*n*10) structures. Peak overlapping is tentatively ascribed to the short potential window in which Pb UPD occurs on copper. The adsorption and desorption of Pb on copper single crystals occur between −0.25 V and −0.37 V *vs.*

SCE, *i.e.* before Pb bulk deposition starts at *ca.* −0.50 V *vs.* SCE.[26,34]

Nevertheless, Pb UPD was still used to evaluate the electrochemical or electroactive surface area (ECSA), as it exhibits intense voltammetric features and low capacitive currents, thereby minimising errors during charge integration.[33] The procedure used to calculate the ECSA is summarised in the SI, and the resulting roughness factors (RFs) for each surface are listed in Table S1. The RFs obtained were 1.05 for $E_R = -0.60$ V, 1.24 for $E_R = -1.30$ V, and 1.27 for $E_R = -1.0$ V. According to the FE-SEM analysis, E_R values of −0.60 V and −1.30 V tend to generate structures with more undercoordinated sites than at E_R of −1.00 V, yet this does not translate into a higher RF. A plausible explanation is that at E_R of −1.00 V the modified surface appears more covered by deposited structures than at the other reduction potentials. This interpretation aligns with the observation that the (111) feature is more suppressed at −1.00 V (Fig. S3F), particularly compared to the modification at −0.60 V, which shows the lowest RF.

Electrochemical surface characterisation with NaCl

To better decouple the contributions of steps and terrace sites on refaceted Cu(111) surfaces prepared at different E_R, voltammetric fingerprints were recorded in 0.1 M NaCl electrolyte. The use of NaCl enables the identification of characteristic voltammetric profiles of Cu(*hkl*) electrodes because copper is weakly active towards HER in neutral NaCl solution, and chloride adsorption is structure sensitive. Consequently, blank CVs for copper single crystal electrodes exhibit characteristic features between −0.30 V and −1.20 V *vs.* SCE.[13] To identify the voltammetric features associated with steps and terraces, measurements were carried out on a series of well-defined stepped Cu surfaces (Fig. 2).[13,35] The Lang–Joyner–Somorjai (LJS) notation was employed to describe these surfaces. In this nomenclature, a surface denoted as Cu(S)[$n(hkl) \times (h'k'l')$] consists of (*hkl*) terraces that are *n* atomic rows wide, separated by monoatomic steps with orientation ($h'k'l'$). The symbol (S) following Cu indicates a stepped surface.

In Fig. 2, the features of the (111), (110) and (100) basal planes are denoted as B1, B2, and B3, whereas the features originated from steps in high index Cu(S)[$n(100) \times (110)$], and Cu(S)[$n(100) \times (111)$] facets are labelled as S1, S1′, S2 and S2′. Fig. 2A shows the voltammetric profiles of the low-index facets, Cu(111) and Cu(110) electrodes, as well as the corresponding turning point surface, Cu(331). This analysis helps determine where defects, such as (110) steps, appear in the CV relative to the (111) terraces, allowing assessment of how potential pulses cause surface roughening or preferential faceting. In Fig. 2A, the (111) facet presents a reversible peak (B1) at −0.89 V. If the cathodic sweep is enlarged to −1.20 V, a second feature centred at −0.60 V emerges in the anodic scan of the (111) voltammogram. A similar feature also appears in other electrolytes and has been ascribed to an electrolyte and potential-driven reconstruction of Cu(111).[36–38] The features of the Cu(110) electrode appear centred at rather positive potential values. In the anodic sweep, the (110) facet has a sharp peak (B2) at −0.49 V, and the counter-feature in the cathodic sweep is broad and centred at −0.53 V. The turning point electrode, Cu(331) or Cu(S)[2(111) × (110)] surface, shows two main features. The first, at −0.53 V, matches nearly well with the (110) facet and is associated with steps in a Cu(S)[$(n-1)(111) \times (110)$] surface. The second broad peak, at −0.86 V, nearly aligns with the (111) facet. Fig. S4 contains ideal hard-sphere models to illustrate the atomic distribution of different turning point surfaces, including the (331) facet.

Fig. 2B and C show the voltammetric response of Cu(S)[$n(100) \times (h'k'l')$] stepped surfaces characteristic of the [01$\bar{1}$]

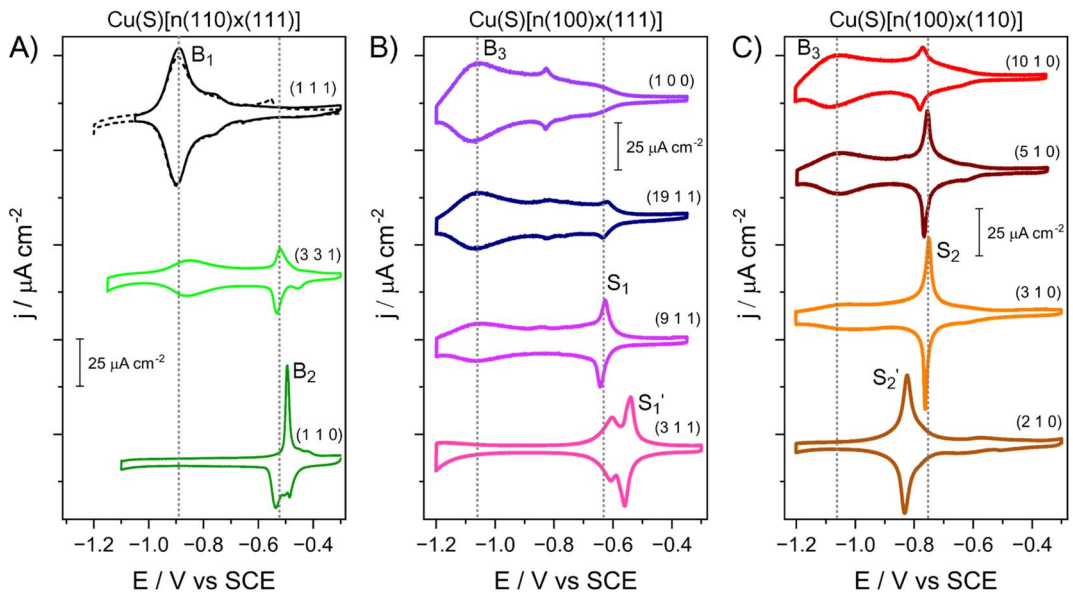

Fig. 2 Blank CVs of different copper single crystals in 0.1 M NaCl at 50 mV s^{-1}: (A) (111), (331), and (110); (B) (100), (19 1 1), (911) and (311); and (C) (10 1 0), (510), (310), and (210).

(Fig. 2B) and [$\bar{1}$00] (Fig. 2C) crystallographic zones. Fig. 2B compares the CVs for several Cu(S)[n(100) × (111)] or (2n−1 1 1) surfaces with the Cu(100) basal plane. These stepped surfaces are Cu(19 1 1), Cu(911), and Cu(311), corresponding to n = 10, 5, and 2, respectively. On the other side, Fig. 2C shows the CVs for several (n10) or Cu(S)[n(100) × (110)] surfaces: (10 1 0), (510), (310) and (210) single crystal electrodes, with n = 10, 5, 3 and 2, respectively. Cu(100) (Fig. 2B) displays a main broad peak labelled as B3, centred at −1.06 V. This feature decreases in intensity as the step density in both Cu(S)[n(100)x(111)] and Cu(S)[n(100)x(110)] surfaces increase and disappears for the respective turning point (n = 2) of each zone; (311) and (210) single crystal electrodes. Cu(S)[n(100)x(111)] surfaces (Fig. 2B) show a second peak centred at −0.64 V (labelled as S1) that becomes sharper as the step density increases. Similarly, on the (n10) group of surfaces, a sharp peak at −0.75 V (denoted as S2) emerges when the step density increases. This electrochemical behaviour indicates that S1 and S2 features correspond to step contributions in Cu(S)[n(100) × (111)] and Cu(S)[n(100) × (110)] surfaces, likely related to chloride specific adsorption on these sites.

The turning points of the [01$\bar{1}$] and [$\bar{1}$00] zones show a voltammetric behaviour that deviates from that of the other stepped surfaces within the same crystallographic zone, which contain (100) terrace sites. The (311) has two peaks in the region of the steps: the first one (S1′) at −0.53 V and the second one at −0.60 V (S1). The CV of the (210) facet contains one single sharp peak (S2′) at −0.82 V, shifted to more negative values compared to S2 (−0.75 V) in (310), (510), and (10 1 0) single crystals. The potential of peak S2' coincides with the two sharp, small peaks observed on the (100) facet in Fig. 2B, which are attributed to minor defects or surface reconstruction. As with other metals, such as Pt, the actual structure of stepped copper surfaces can be more complex, and faceting may occur during electrochemical processes, leading to the formation of higher steps compensated by wider terraces.[39] Turning point surfaces and densely stepped surfaces are particularly prone to faceting and step bunching due to their high surface energies. This fact could affect the voltammetric shapes of the turning point electrodes. It cannot be discarded that the use of the electropolishing method to pretreat the single crystal electrodes could introduce a slight disorder in the turning point surfaces, affecting their voltammetric profiles, as single crystal electrodes are sensitive to the surface pretreatment.[40,41]

Notably, Wandelt and co-workers[18] used scanning tunnelling microscopy (STM) to investigate whether the adsorption of chloride on copper basal planes in mildly acidic media induces surface reconstruction. Ordered adsorbed ($\sqrt{3}$ × $\sqrt{3}$)R30° and c(2 × 2) chloride structures were observed on Cu(111) and Cu(100), respectively. Cu(110) exhibited severe reconstruction and the formation of directional stripes, although the surface recovered when scanning to negative potentials. These STM studies confirmed that chloride adsorption is both facet- and potential-dependent. The pronounced reconstruction of Cu(110) was attributed to the greater accessibility and lower electrostatic repulsion of chloride anions on this surface, as its geometry is more open and electropositive than the other two basal planes.[18] As far as it is known, there are no STM studies on chloride adsorption/desorption in high-index facets. Verification of adsorbed chloride structures and surface reconstruction on high-index facets requires further studies with *in situ* STM. Notably, CVs in Fig. 2 remain stable upon consecutive cycles, suggesting that either chloride adsorption or reconstruction phenomena are intrinsic to each facet,[16] thereby allowing sites of different geometry to be distinguished by cyclic voltammetry in NaCl.

Addressing the terrace-to-step ratio in refaceted Cu(111)

After confirming that NaCl enables the distinction between terrace and step sites of different geometries, it was employed to evaluate the facet distribution on refaceted Cu(111) surfaces at different E_R. Fig. 3A contains the blank CVs in NaCl of the pulsed-refaceted Cu(111) electrode at E_R = −1.30 V, −1.00 V and −0.60 V for 300 s. All the CVs display well-defined, separated peaks which potentials match well with those of low-index facets and step contributions on high-index surfaces shown in Fig. 2. For clarity, labels B1–B3 were added to denote low-index facets and S1–S2 to indicate step sites in Fig. 3. In all three modifications, a noticeable decrease in the (111) peak contribution (B1) is observed, accompanied by the emergence of peaks S2 and S2′, corresponding to step sites in a [n(100) × (110)] geometry. This result supports the formation of (n10) structures covering the (111) substrate, in line with the SEM analysis in Fig. 1. Additionally, a new feature centred at S1 appears, suggesting the formation of (111) steps or defects adjacent to a (100) terrace. The current peaks associated with step features (S1, S2) are similar across all three modifications, with S2 being more prominent than S1 at E_R of −1.00 V and −1.30 V. Notably, peak B2, related to (110) sites, is the weakest feature in all cases. Regarding the evolution of (100) terraces denoted as peak B3 in Fig. 3, the surface modified at −1.00 V displays the most intense peak, followed by those modified at −1.30 V and −0.60 V. These results suggest that pulsing the copper electrode in NaCl does not simply induce (110) defects on a (111) plane. Instead, it preferentially induces the formation of (110) and (111) steps or defects adjacent to (100) terraces, and the density of steps or defects respective to (100) terrace sites is dependent on the applied reduction potential.

To better evaluate the formation of (100) terraces relative to the quantity of steps and other defects, the charge associated with (100) domains, (111) domains, and step or defect sites was calculated from the anodic or positive scans of the modified Cu(111) electrodes. For the charge integration, the experimental curves were simulated by fitting data obtained from the CVs of single facet and stepped surfaces shown in Fig. 2. The resulting simulated curves, which combine the contributions from these single crystal surfaces, are presented in Fig. S5. A detailed description of the curve fitting procedure is provided in the SI. The (111) and (100) contributions for the modified Cu(111) electrodes were then estimated by integrating the charge under the fitted curves corresponding to these two facets. For simplicity, the remaining portion of the voltammetric curve was assumed to contain the contributions of steps (including (110)

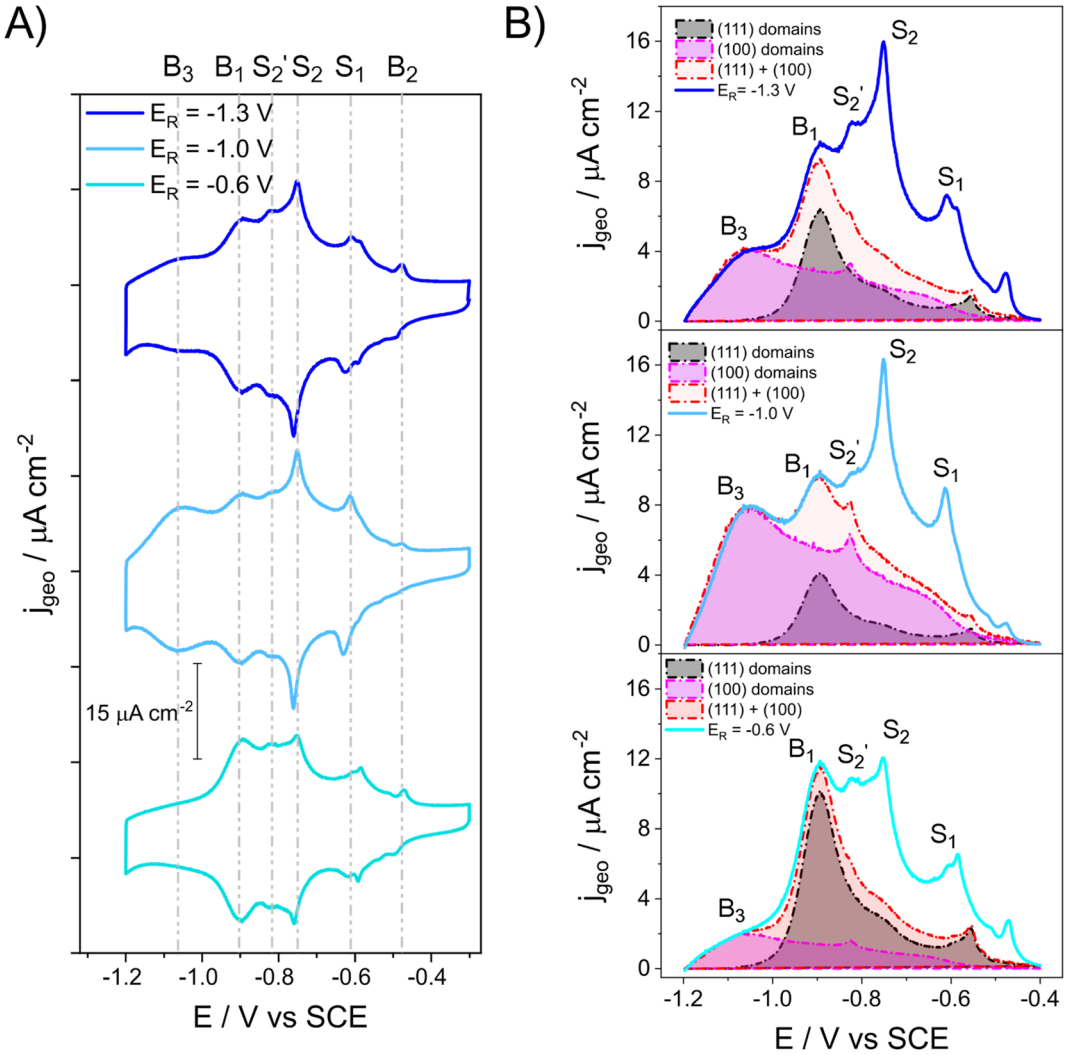

Fig. 3 (A) CVs of modified Cu(111) surfaces at different E_R, recorded in 0.1 M NaCl at 50 mV s^{-1}. (B) Anodic scans of the modified Cu(111) surfaces at the three mentioned E_R in (A), that were used to determine the contribution of (100) and (111) terraces, as well as the contribution of low coordinated sites. The voltammetric area involving the (111) and (100) terraces is highlighted in purple and black, respectively, to better illustrate the evolution of facet distribution at each E_R. The total area for both (111) and (100) terrace sites is shown in red in each case to distinguish it from the area accounting for steps and defects. In the CVs of refaceted Cu(111) surfaces, geometric current density (j_{geo}/μA cm^{-2}) refers to current divided by the geometric surface area of the electrodes without considering the RF.

sites) and other defects derived from the refaceting process. Accordingly, the charge associated with these features was determined as:

$$Q_{steps} = Q_{total} - Q_{(100)} - Q_{(111)} \quad (1)$$

Fig. 3B shows the anodic curves of the pulsed-modified Cu(111) surface obtained at the three different potentials, highlighting the (111) and (100) terrace contributions in black and purple, respectively, along with the fitted curve resulting from their combination. The integrated charges for (100), (111), and step contributions are summarised in Table S2.

The surface modified at $E_R = -0.60$ V shows the lowest proportion of (100) domains (28% of the total charge), followed by $E_R = -1.30$ V (37%), with step and defect contributions of 38% and 40%, respectively. The corresponding terrace-to-step charge ratios ($Q_{(100)}/Q_{steps}$) in the modified surfaces are 0.7 and 0.9 for E_R of −0.60 V and −1.30 V, respectively. The highest proportion of (100) domains is achieved at $E_R = -1.00$ V, representing 57% of the total surface charge, whereas the density of steps and defects decreases to 29%, yielding a terrace-to-step charge ratio of 2.0. These results indicate that both fast and slow deposition rates ($E_R = -1.30$ and −0.60 V) favour the formation of steps or defect-rich Cu[n(100)x($h'k'l'$)] structures, while a moderate deposition rate ($E_R = -1.00$ V) promotes surface faceting and the growth of slightly larger (100) terrace domains. Fig. 3 also shows that the (111) facet contribution decreases considerably at $E_R = -1.00$ V, accounting for a charge ($Q_{(111)}$) of *ca.* 14 μC cm^{-2}. The (111) facet contribution accounts for *ca.* 23 μC cm^{-2} at $E_R = -1.30$ V and 29 μC cm^{-2} at $E_R = -0.60$ V. This result indicates that reduction potentials around −1.00 V not only facilitate the formation of slightly larger (100)

terraces but also increase the coverage of newly formed structures.

A tentative explanation for the effect of applied reduction potential and deposition rate on surface refaceting of copper can be proposed based on previous studies on particle nucleation and growth.[42,43] Rapid nucleation limits particle growth and surface faceting due to rapid consumption of precursor during nucleation, leading to the formation of highly undercoordinated or high-index facet structures. When the reduction potential becomes less negative, nucleation becomes moderate, growth is more balanced, and the system has time to restructure. Under these conditions, low-index facets with lower surface energies and greater thermodynamic stability evolve. If the reduction potential becomes too mild, the growth rate becomes excessively slow, leading to smaller defect-rich particles and poor surface coverage. Further clarification on how chloride and reduction potential influence nucleation and growth mechanisms during pulse-refaceting of copper requires *in situ* microscopy to monitor morphological changes over time.[44,45]

Pulse-mediated surface refaceting of a copper polycrystalline electrode

The applicability of the potential-pulse method to modify a Cu(poly) surface was also explored, evaluating how different underlying crystallographic orientations influence the growth of new structures. Fig. 4A shows the blank CV in NaCl of the pristine surface (left) and after modification at $E_R = -1.00$ V (right). Fig. 4B displays a real picture of the Cu(poly) electrode after applying potential pulses at $E_R = -1.00$ V, revealing that it originally contains four grains, labelled as A, B, C, and D in Fig. 4B.

Cyclic voltammograms of pristine Cu(poly) were recorded in two different potential windows: a short potential window between −0.30 V and −1.10 V *vs.* SCE and a long window between −0.30 V and −1.20 V *vs.* SCE. The voltammetric response of the pristine Cu(poly) (Fig. 4A, left) indicates that the dominant orientation corresponds to the (111) facet, as evidenced by the intense voltammetric feature (i) centred at −0.89 V. The CV is featureless at −1.06 V, indicating the absence of (100) terrace-domains. The sharp pair of peaks centred at −0.82 V (ii) aligns well with the response of the (210) facet (Fig. 2), while the feature at −0.60 V (iii, Fig. 4A) could be related to (100) defect sites in (111) terraces, as the surface does not contain (100) terraces. This feature is slightly sharper when the cathodic sweep is extended to −1.2 V. Additional small peaks in the anodic potential range between −0.55 V and −0.42 V are difficult to assign but may correspond to other defect structures or low coordinated (110) sites.

EBSD was employed to further elucidate the crystallographic orientation of each grain. The EBSD analysis of Fig. 4B reveals that the precise orientation of grain A is (57 53 64), which corresponds to approximately a (111) orientation. Grain C, the second largest, has a (89 47 1) ∼ (210) orientation, which is likely linked to peak (ii) in the CV. Grain B shows a (79 49 37) ∼ (854) orientation, characterised by (111) terraces ($n = 3$) with (100) steps, likely related to peak (iii), and kink sites. Finally, grain D presents a (82 55 18) ∼ (431) orientation, a highly kinked surface containing (111) terraces ($n = 3$) with (110) steps and kinks. The EBSD results also confirm the absence of (100) terraces, consistent with the blank CV in NaCl for Cu(poly) (Fig. 4A, left panel). Overall, the combined EBSD map and voltammetric analyses demonstrate that blank CVs in NaCl are effective for identifying terrace and step geometries of different orientations. However, kink sites are more difficult to distinguish electrochemically and require complementary surface characterisation techniques, such as EBSD.

The right panel of Fig. 4A shows the CV in NaCl of the modified Cu(poly) at −1.00 V for 180 s. Interestingly, the blank CV of refaceted Cu(poly) shows a peak distribution similar to that of the modified Cu(111) at the same E_R, but after applying potential pulses for a shorter period of time. Modifications performed at E_R of −1.30 V and −0.60 V for 180 s on Cu(poly) also exhibit analogous voltammetric features to those observed on modified Cu(111) for 300 s, as shown in Fig. S6. The faster modification of Cu(poly) compared to Cu(111) was attributed to the presence of grain boundaries and kinks, illustrating that refaceting kinetics are structure-sensitive. Fig. 4C presents SEM images of two regions of the electrode modified at −1.00 V, where three grains converge, clearly illustrating the grain boundaries. Each modified grain has a distinct morphology, highlighting the influence of substrate orientation on the growth of new structures.[6] Fig. S6C shows a SEM image of the pristine Cu(poly) surface, confirming the relative flatness of the grains prior to modification.

To gain an in-depth understanding of the effect of each grain orientation on the formation of shaped structures and to explain the morphological differences observed in Fig. 4, the following analysis was conducted. A cubic particle with (100) facets was simulated (Fig. 5) and sequentially intersected with planes corresponding to each grain orientation, thereby modelling epitaxial particle growth. Fig. 5 also illustrates the atomic configuration of the identified grain orientations, showing the atomic arrangement in the stepped (C) and kinked (B and D) grains. SEM images of the respective modified grains are shown alongside the models for comparison.

Grain A, with a (111) orientation, develops a well-defined pattern of triangular pyramids, similar to Fig. 1A, though even more distinctly triangular. Stepped surfaces, such as grain C, and those with a low density of kinks, such as in grain B, tend to form symmetric morphologies. Conversely, highly kinked surfaces, such as grain D with a (431) orientation, display asymmetric stepped morphologies arising from the chiral nature of the kinks. The strong agreement between the simulated particle growth and the experimentally observed morphology structures in the SEM confirms that growth occurs epitaxially, governed by the crystallographic plane angle, while the applied reduction potential and electrolyte anions dictate the resulting facet formation on copper.

Electrochemical HMF oxidation and reduction on refaceted copper

After showing that the SWP method produces either short or slightly larger (100) terraces, the next step was to assess whether

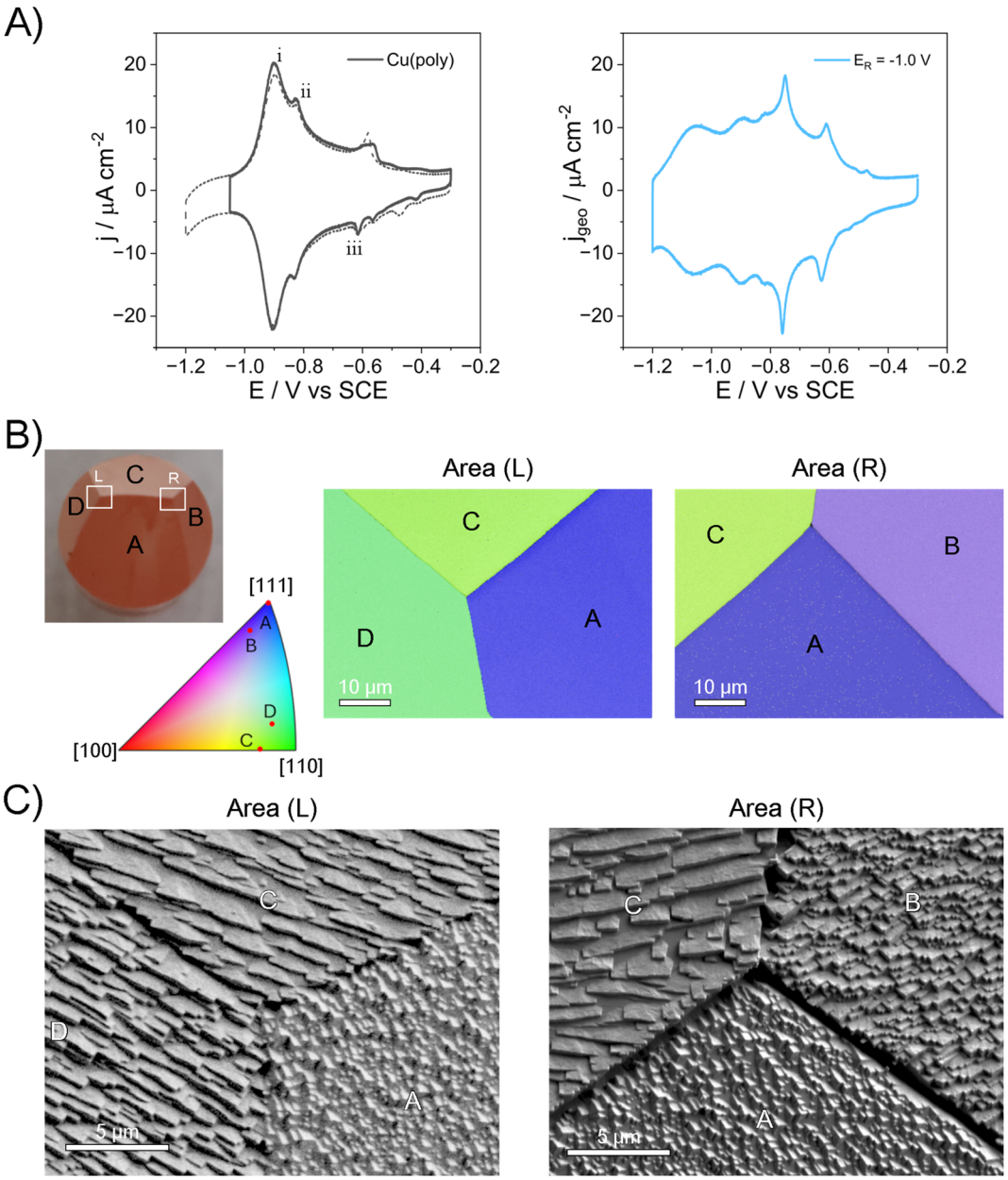

Fig. 4 (A) CVs of Cu(poly) recorded in 0.1 M NaCl solution at 50 mV s^{-1}: (left side) after electropolishing; (right side) after modification at E_R of −1.00 V for 180 s. (B) Includes: a real picture of the Cu(poly) after being refaceted at $E_R = -1.00$ V illustrating its four grains labelled as A, B, C and D; an EBSD map of the electropolished Cu(poly), *i.e.*, before being modified; and the stereographic triangle for face-centred cubic (fcc) structures showing the approximate orientation of the four Cu(poly) grains; the stereographic triangle has the colours code used to distinguish crystalline orientations in the EBSD map. (C) SEM images of two different grain boundary regions of the modified polycrystalline electrode at −1.00 V.

tuning the ratio of terraces, steps, and defects can be used to tailor the electrocatalytic properties of copper. To achieve this, the oxidation and reduction of HMF were investigated in alkaline media. Copper is active for both processes, making it an effective dual probe to evaluate variations in performance resulting from electrochemically induced structural modifications.[20,29] Both HMF oxidation and reduction initiate within the potential region where neither copper oxidation nor hydrogen evolution reactions occur; thereby, the obtained electrocatalytic response can be mainly attributed to HMF conversion. To evaluate the electrocatalytic response of HMF oxidation on modified Cu(111) and Cu(poly) electrodes, cyclic voltammograms were recorded between 0.00 V and 0.50 V *vs.* RHE (Fig. 6A and C). To assess onset potentials in HMF reduction on copper, linear sweep voltammograms (LSVs) were recorded in the potential region between 0.05 V and −0.40 V *vs.* RHE (Fig. 6B and D). Experiments were performed at pH slightly below 13, in 0.05 M NaOH solution, to minimise the chemical degradation of HMF over the course of each experiment.[27] Before measuring the catalytic response of copper towards HMF oxidation and

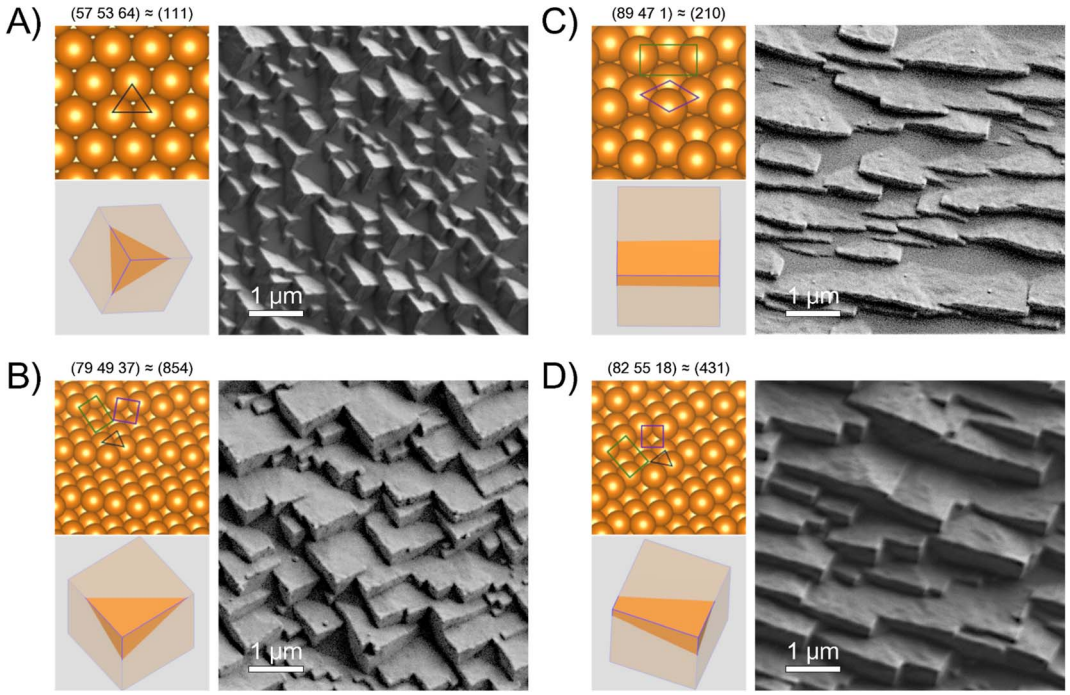

Fig. 5 Atomic structures of the different grain orientations in the Cu(poly) and simulations of particle growth, as well as SEM images of the grain domains modified at E_R of −1.00 V *vs.* SCE. In the figure, the precise crystalline orientation and the approximate orientation with Miller Indices are indicated on top of the atomic structures. (A) (111) grain; (B) (854) grain; (C) (210) grain; and D) (431) grain. To address the morphology of the formed particles on each grain, we simulated a cubic particle with (100) facets and intersected it with a plane with the orientation of the corresponding grain, simulating epitaxial particle growth.

reduction, blank CVs of each modified Cu(111) and Cu(poly) electrode at different E_R values were recorded, which are depicted in Fig. S7. In NaOH-blank CVs, the (111) and (100) peak contributions appear at 0.15 and −0.20 V *vs.* RHE, respectively.[28] The surfaces modified at −1.00 V show more intense (100) peaks, consistent with the results in NaCl. Unlike NaCl electrolyte, step and defect features overlap in the upper region of the voltammogram in NaOH, complicating the distinction of individual step contributions on refaceted copper.[3,46] The activities of the modified Cu(111) and Cu(poly) substrates towards HMF oxidation and reduction were normalised by the ECSA to provide an approximate measure of the intrinsic activity related to the surface site structure. The ECSA for each electrode was obtained from Pb UPD measurements. In Fig. S8, HMF oxidation and reduction CVs were plotted against geometric activity, or current normalised by electrode area, to illustrate the complete activity change affected by site geometry and roughness factor effects.

Fig. 6A plots the HMF partial oxidation on modified Cu(111) at E_R of −1.30 V, −1.00 V and −0.60 V, and the results were compared with those of the bare Cu(111) facet. HMF oxidation voltammograms display a progressive current increase in the anodic scan, reaching a maximum followed by a current decay at approximately 0.45 V. Upon the reverse scan, the current increases again, overlapping with the anodic response. This behaviour has been previously attributed to metallic copper acting as the active phase responsible for the partial oxidation of the aldehyde group in HMF. During partial oxidation of HMF, copper only produces 5-hydroxymethyl furoic acid (HMFCA), which is the product favoured at lower overpotentials. At a potential above 0.5 V, where 2,5-furandicarboxylic acid (FDCA) is produced, copper is oxidised and deactivated.[20,47] Cu(111) single facet presents a high onset potential and low activity for HMF oxidation, whereas the three modified surfaces display enhanced activity. Among them, the surface modified at −0.60 V presents the highest current density, followed by those prepared at −1.30 V and by −1.00 V. Chico-Mesa *et al.* recently examined the oxidation of HMF on gold single crystals and reported that highly stepped surfaces exhibited higher activity toward aldehyde oxidation,[47] due to their negligible energy barrier for the C–H bond activation of the gem-diol intermediate.[48] In line with these results, previous studies on copper have shown that surfaces rich in defects and low-coordinated sites, such as rough foils, oxide-derived electrodes and nanoparticles, are highly active for the partial oxidation of HMF.[20,49] The analysis in Fig. 6B also indicates that low-coordinated sites in refaceted copper control partial oxidation of HMF on copper, whereas (100) and (111) sites have a minor contribution to the catalytic response.

Fig. 6B presents LSVs of the reduction of HMF on Cu(111) surfaces modified at the same reduction potentials. The HMF reduction on copper follows a distinct structure–activity trend compared to its oxidation. In the negative scan, the Cu(111) surface modified at −1.00 V exhibits the lowest onset potential, shifted by approximately 100 mV toward lower potentials at a current of −1 mA cm^{-2} relative to the pristine Cu(111). In

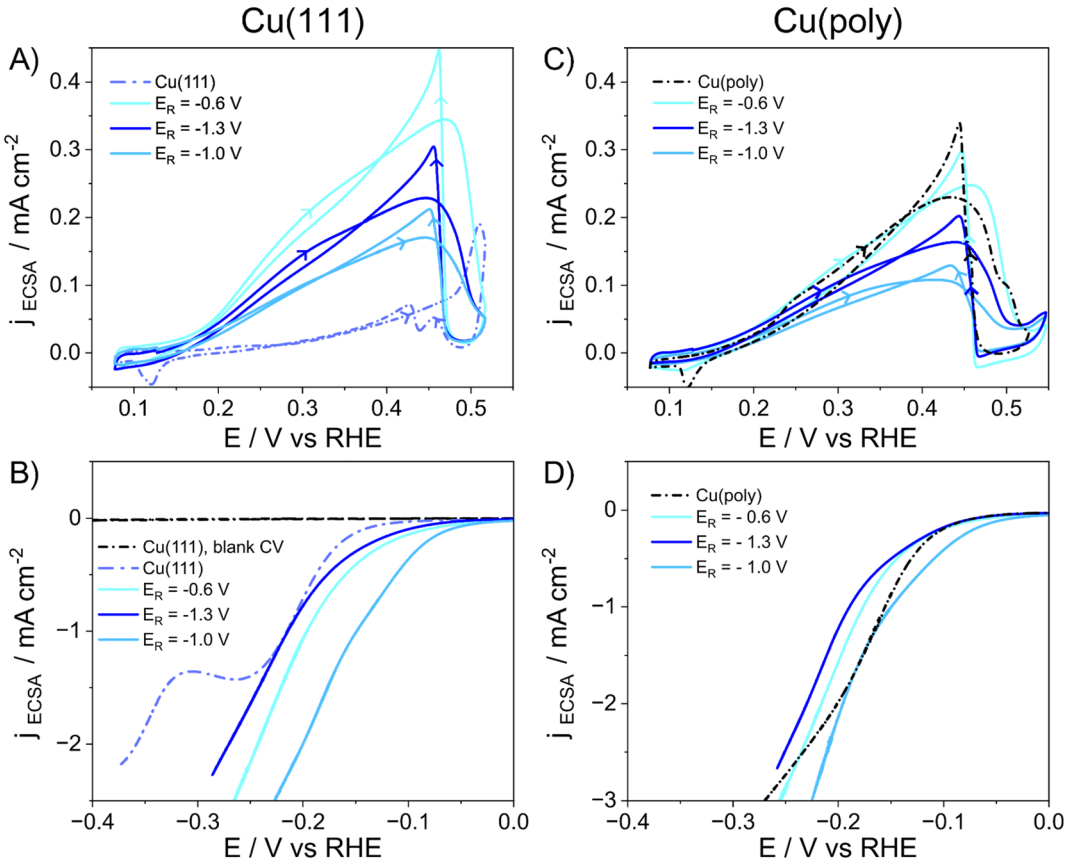

Fig. 6 CVs and LSVs for the oxidation and reduction of 50 mM HMF in 0.05 M NaOH solution at 10 mV s^{-1}. (A) and (B) show HMF oxidation and reduction on bare Cu(111) and modified Cu(111) at three different E_R; (C) and (D) show HMF oxidation and reduction on bare Cu(poly) and modified Cu(poly) electrodes at the same E_R. HMF reduction curves in (B) and (D) are manually IR corrected (correction of 100%), whereas the HMF oxidation in (A) and (C) are not IR corrected to avoid distorting the voltammetric sharp peak in the cathodic scan.

contrast, the modified surfaces at −1.30 V and −0.6 V show more minor shifts of 3 and 20 mV, respectively, at the same current density. The lowest onset potential for the Cu(111) modified at −1.00 V indicates that slightly larger (100) domains, and not only steps or defects, are active towards the hydrogenation of the carbonyl group of HMF. This observation tentatively suggests that (100) terrace sites adjacent to a step or defect site may help stabilise and adsorb a key reaction intermediate, thus decreasing the onset potential in alkaline media.

The CVs for HMF oxidation and reduction on Cu(poly) electrodes modified at the same E_R values (−1.30 V, −1.00 V, and −0.60 V) appear depicted in Fig. 6C and D. For HMF oxidation (Fig. 6C), the surface modified at −0.60 V shows the highest intrinsic activity, clearly surpassing the performance of the Cu(poly) modified at −1.00 V. However, the unmodified Cu(poly) shows nearly comparable activity to the surface modified at −0.60 V. For HMF reduction (Fig. 6D), the surface modified at −1.00 V still displays higher intrinsic currents and lower onset potentials in the negative scan, but the difference with the pristine Cu(poly) is little because this Cu(poly) reduces HMF at relatively low overpotentials. The intrinsically low onset potential and high activity of the Cu(poly) for HMF reduction and oxidation are attributed to the presence of defects and the existence of two kinked facets, which are known to act as active sites in catalysis.[15,50] Overall, the voltammograms of the modified Cu(poly) electrodes follow similar structure–activity trends as those observed in Cu(111) electrodes modified at the same E_R, highlighting an acceptable reproducibility of the pulsed-mediated refaceting method across distinct substrates.

In addition to the negative LSVs of the reduction of HMF on refaceted Cu(111) and Cu(poly) (Fig. 6B and D), full cyclic voltammograms displaying both the negative and the reverse or positive scan of this reaction were included in Fig. S8. The reverse or positive scan in HMF reduction shows slightly lower current than the negative scan, indicating that activity on copper decreases with time. This activity inhibition is more pronounced on pure Cu(111) and on pure Cu(poly) than on refaceted copper. Surfaces modified at E_R of −0.60 V and −1.30 V, which contain more defect-rich structures, showed lower current deactivation compared to the same surfaces modified at −1.00 V.

Unlike the oxidation of HMF, which selectively yields 5-hydroxymethylfuroate,[20] the reduction of HMF can produce a broader distribution of products. A previous study on the electrochemical reduction of HMF on copper showed that, at low to moderate applied overpotentials, Cu(110) single crystal

selectively forms 2,5-bis(hydroxymethyl)furan (BHMF). In contrast, Cu(100) single crystal promotes the dimerisation pathway, forming 5,5′-bis(hydroxymethyl)hydrofuroin (BHH) as well as BHMF.[29] A similar facet-dependent catalytic trend has been reported for CO_2 reduction. In CO_2 reduction, Cu(100) terraces with steps reduce CO_2 at lower potentials and enhance the formation of C_2^+ products[51,52] *via* the generation of a protonated OCCOH* dimer intermediate.[53] For HMF reduction, density functional theory (DFT) calculations suggest a common radical intermediate for the BHH and BHMF dimer pathways, corresponding to HMF with a protonated aldehyde oxygen group (R–COH*). Notably, it has been suggested that the HMF reduction reaction is limited by both the adsorption of HMF reactants and intermediates and the desorption of products.[29] Indeed, previous studies have shown that conversion efficiency on Cu(110) is higher than on Cu(100) over time due to relatively weaker product adsorption on Cu(110), whereas Cu(100) tends to accumulate byproducts on the surface.[21,29] This facet-dependent behaviour could explain why refaceted Cu(111) at $E_R = -1.00$ V, with more (100) sites, initially reduces HMF at considerably lower overpotentials than the other refaceted surfaces, but exhibits slightly greater current hysteresis upon scan reversal. To further support these observations, we have included the cyclic voltammograms of HMF reduction on Cu(100) and Cu(110) in Fig. S9. Fig. S9 shows that Cu(100) exhibits both the lowest onset potential and the most pronounced current hysteresis.

Finally, the stability of refaceted Cu(111) was tested during HMF reduction by recording chronopotentiometric transients at a constant current density of 2.5 mA cm^{-2} for at least 30 minutes (Fig. S10A). This applied current density is on the order of that recorded by cyclic voltammetry on copper and in the potential range between −0.20 V and −0.40 V *vs.* RHE (Fig. 6B and D). The electrode potential was then monitored over time. Specifically, Cu(111) modified at $E_R = -0.60$ V and $E_R = -1.00$ V were assessed. At this conversion rate, the potential of both refaceted Cu(111) surfaces remained relatively stable. The surface modified at $E_R = -1.0$ V exhibited a slightly lower electrode potential during the reaction. Fig. S10A also shows the chronopotentiometry of Cu(poly), which primarily contains (111) terraces together with kink or step sites. Cu(poly) displays a higher overpotential than refaceted Cu(111), and moderate deactivation as the electrode potential becomes more negative over time. The blank CVs of Cu(111) refaceted at −1.00 V, before and after the chronopotentiometry experiments (Fig. S10B), were recorded in 0.1 M NaCl. Essentially, the same voltammetric features were observed before and after HMF electrolysis, with minimum surface contamination after 30 minutes of reaction. This result indicates that HMF reduction does not significantly alter facet distribution on refaceted copper. In Fig. S10C and D the chronopotentiometric transients for Cu(111) and Cu(100) single crystals are shown. Interestingly, both Cu(111) and Cu(100) single crystals suffered severe deactivation. Cu(111) deactivated in less than a minute, whereas Cu(100) did so after a few minutes. The electrode potential of both surfaces decreased to values where hydrogen evolution occurs instead.[54]

These results show that defects and steps on refaceted copper prevent surface deactivation at moderate HMF reduction rates, possibly by facilitating desorption of products and avoiding surface poisoning. On the other hand, voltammetric results show that the terrace-to-defect ratio dictates the onset potential of the reduction reaction, which may be influenced by the different affinity of HMF reactants and intermediates for terrace and step sites. It is worth noting that experiments were performed under non-rotating conditions. Thus, future studies should evaluate the influence of mass transport conditions on the diffusion of both reactants, intermediates, and products to optimise performance over extended periods of time. Product characterisation lies beyond the scope of this work, which instead focuses on correlating copper surface restructuring with changes in overpotential and catalytic activity at the beginning of the reaction. Future work will scale up the proposed refaceting methods to tune the facet distribution of larger electrodes, aiming to achieve higher sensitivity during product detection, and address how different terrace-to-step ratios influence product distribution.

Conclusions

Overall, this work introduces the use of blank CVs in NaCl as an effective approach to decouple the voltammetric contributions of terrace and step sites in single crystal copper facets, thereby providing expanded insights into the crystallographic domains present in refaceted copper surfaces. The combined analysis of CVs and SEM reveals that, during the application of potential pulses, chloride plays a key role in stabilising and promoting the formation of sites with (100) geometry. However, the development of step-rich or terrace-rich structures depends on the deposition rate. Fast deposition rates, which enhance nucleation, primarily lead to the formation of (n10) facets and [n(100) × (111)] geometries with high step or defect density. In contrast, moderate deposition rates favour surface faceting and reorganisation, resulting in increased surface area, higher surface coverage, and the formation of larger (100) terrace domains and lower defect density. When the deposition rate is too slow, the induced structures lack sufficient time to evolve, resulting in a more uncovered (111) surface and considerably smaller, defect-rich hexagonal clusters. Further clarification of these possible growth mechanisms will require *in situ* electrochemical SEM to monitor the morphological evolution over time at distinct E_R values. This study also demonstrates that tailoring the terrace-to-step or defect ratio significantly influences the catalytic performance of copper. Comprehensive electrochemical surface characterisation of refaceted or nanostructured copper is therefore essential to identify the specific combinations of site geometries that govern oxidation and reduction reactions on copper.

Author contributions

Vicente Pascual Llorens: conceptualisation (Cu(poly) analysis with EBSD), investigation (copper refaceting, catalysis, single-crystal study), methodology, formal analysis, data curation,

visualisation, writing – original draft. Lorena Chico Mesa: investigation (single-crystal study, catalysis), methodology, formal analysis, visualisation, writing, and reviewing the original draft. Michael Musi: investigation (Cu(poly) analysis with EBSD), methodology, formal analysis, data curation, visualisation, reviewing – original draft. Rosa M. Arán-Ais: conceptualisation (single-crystal study, catalysis), supervision, methodology, project administration, resources, funding acquisition, writing – and reviewing original draft. Paula Sebastián-Pascual: conceptualisation (copper refaceting, NaCl voltammetric probe, catalysis), formal analysis (simulated NaCl blank CVs on refaceted copper), supervision, methodology, project administration, resources, funding acquisition, writing – and reviewing original draft.

Conflicts of interest

There are no conflicts of interest to declare.

Data availability

The data supporting this article have been included as part of the supplementary information (SI). See DOI: https://doi.org/10.1039/d6ta00313c.

Acknowledgements

VPL and PSP thank the Wallenberg Initiative Materials Science for Sustainability (WISE) funded by the Knut and Alice Wallenberg Foundation for financial support (WISE-F01-06-S) VPL also acknowledges the Asociación de Científicos Españoles en Suecia (ACES) and the Fundación Ramón Areces for financial support during the exchange in Alicante University. LCM and RMAA acknowledge support from Ministerio de Ciencia, Innovación y Universidades through grants PREP2022-000182 and RYC2022-038206-I, respectively. PSP also thanks Vetenskapsrådet (The Swedish Research Council, nr 2024-04131) and Göran Gustafsson Stiftelse (nr 2515) for providing funding. We thank KTH and 2MIlab for microscopy facilities provided to perform this project. We also thank Lecturer Albert Serrà Ramos and Professors Juan M. Feliu and Elvira Gómez, who provided valuable discussions.

References

1 C. S. Le Duff, M. J. Lawrence and P. Rodriguez, *Angew. Chem., Int. Ed.*, 2017, **56**, 12919–12924.
2 K. W. Kimura, K. E. Fritz, J. Kim, J. Suntivich, H. D. Abruña and T. Hanrath, *ChemSusChem*, 2018, **11**, 1781–1786.
3 R. M. Arán-Ais, F. Scholten, S. Kunze, R. Rizo and B. Roldan Cuenya, *Nat. Energy*, 2020, **5**, 317–325.
4 J. Timoshenko, A. Bergmann, C. Rettenmaier, A. Herzog, R. M. Arán-Ais, H. S. Jeon, F. T. Haase, U. Hejral, P. Grosse, S. Kühl, E. M. Davis, J. Tian, O. Magnussen and B. Roldan Cuenya, *Nat. Catal.*, 2022, **5**, 259–267.
5 N. Tian, Z.-Y. Zhou, S.-G. Sun, Y. Ding and Z. L. Wang, *Science*, 2007, **316**, 732–735.
6 A. J. Arvia, J. C. Canullo, E. Custidiano, C. L. Perdriel and W. E. Triaca, *Electrochim. Acta*, 1986, **31**, 1359–1368.
7 J. Xiao, S. Liu, N. Tian, Z.-Y. Zhou, H.-X. Liu, B.-B. Xu and S.-G. Sun, *J. Am. Chem. Soc.*, 2013, **135**, 18754–18757.
8 L. C. Tănase, M. J. Prieto, L. de Souza Caldas, A. Tiwari, F. Scholten, P. Grosse, A. Martini, J. Timoshenko, T. Schmidt and B. Roldan Cuenya, *Nat. Catal.*, 2025, **8**, 881–890.
9 E. Custidiano, A. C. Chialvo and A. J. Arvia, *J. Electroanal. Chem. Interfacial Electrochem.*, 1985, **196**, 423–427.
10 A. Visintin, W. E. Triaca and A. J. Arvia, *J. Electroanal. Chem. Interfacial Electrochem.*, 1987, **221**, 239–243.
11 N. Tian, Z.-Y. Zhou, N.-F. Yu, L.-Y. Wang and S.-G. Sun, *J. Am. Chem. Soc.*, 2010, **132**, 7580–7581.
12 C. Xiao, N. Tian, W.-Z. Li, X.-M. Qu, J.-H. Du, B.-A. Lu, B.-B. Xu, Z.-Y. Zhou and S.-G. Sun, *CrystEngComm*, 2021, **23**, 6655–6660.
13 V. Pascual-Llorens, A. Serrà-Ramos and P. Sebastián-Pascual, *Electrochim. Acta*, 2025, **518**, 145793.
14 P. M. Couce, T. K. Madsen, E. Plaza-Mayoral, H. H. Kristoffersen, I. Chorkendorff, K. N. Dalby, W. van der Stam, J. Rossmeisl, M. Escudero-Escribano and P. Sebastián-Pascual, *Chem. Sci.*, 2024, **15**, 1714–1725.
15 O. J. Wahab, M. Kang, E. Daviddi, M. Walker and P. R. Unwin, *ACS Catal.*, 2022, **12**, 6578–6588.
16 H. Wang, L. D. B. Mandemaker, J. de Ruiter, X. Yu, W. van der Stam and B. M. Weckhuysen, *Angew. Chem., Int. Ed.*, 2025, **64**, e202424530.
17 N. Hoshi, M. Kato and Y. Hori, *J. Electroanal. Chem.*, 1997, **440**, 283–286.
18 K. Wandelt, in *Encyclopedia of Interfacial Chemistry*, ed. K. Wandelt, Elsevier, Oxford, 2018, pp. 166–181.
19 A. Bagger, R. M. Arán-Ais, J. Halldin Stenlid, E. dos Santos, L. Arnarson, K. Degn Jensen, M. Escudero-Escribano, B. Roldan Cuanya and J. Rossmeisl, *ChemPhysChem*, 2019, **20**, 1–11.
20 T. Wang, L. Tao, X. Zhu, C. Chen, W. Chen, S. Du, Y. Zhou, B. Zhou, D. Wang, C. Xie, P. Long, W. Li, Y. Wang, R. Chen, Y. Zou, X.-Z. Fu, Y. Li, X. Duan and S. Wang, *Nat. Catal.*, 2022, **5**, 66–73.
21 J. Li and N. Kornienko, *Chem. Commun.*, 2021, **57**, 5127–5130.
22 S. Liu, Z. Mukadam, S. B. Scott, S. C. Sarma, M.-M. Titirici, K. Chan, N. Govindarajan, I. E. L. Stephens and G. Kastlunger, *EES Catal.*, 2023, **1**, 539–551.
23 P. Nilges and U. Schröder, *Energy Environ. Sci.*, 2013, **6**, 2925–2931.
24 A. Tiwari, T. Maagaard, I. Chorkendorff and S. Horch, *ACS Energy Lett.*, 2019, **4**, 1645–1649.
25 H. Matsushima, A. Taranovskyy, C. Haak, Y. Gründer and O. M. Magnussen, *J. Am. Chem. Soc.*, 2009, **131**, 10362–10363.
26 G. M. Brisard, E. Zenati, H. A. Gasteiger, N. Markovic and P. N. Ross, *Langmuir*, 1995, **11**, 2221–2230.
27 Y. Ramli, V. Chaerusani, Z. Yang, Z. Feng, S. Karnjanakom, Q. Zhao, S. Li, Y. Li, A. Abudula and G. Guan, *J. Environ. Chem. Eng.*, 2024, **12**, 113666.

28 A. Tiwari, H. H. Heenen, A. S. Bjørnlund, T. Maagaard, E. Cho, I. Chorkendorff, H. H. Kristoffersen, K. Chan and S. Horch, *J. Phys. Chem. Lett.*, 2020, 1450–1455.
29 M. Li, T. Zheng, D. Lu, S. Dai, X. Chen, X. Pan, D. Dong, R. Weng, G. Xu and F. Wang, *J. Energy Chem.*, 2023, **84**, 101–111.
30 K. Kawashima, R. A. Márquez, Y. J. Son, C. Guo, R. R. Vaidyula, L. A. Smith, C. E. Chukwuneke and C. B. Mullins, *ACS Catal.*, 2023, **13**, 1893–1898.
31 W. Zheng, *ACS Energy Lett.*, 2023, **8**, 1952–1958.
32 J. M. Feliu and E. Herrero, *EES Catal.*, 2024, **2**, 399–410.
33 P. Sebastián-Pascual and M. Escudero-Escribano, *J. Electroanal. Chem.*, 2021, **896**, 115446.
34 G. M. Brisard, E. Zenati, H. A. Gasteiger, N. M. Marković and P. N. Ross, *Langmuir*, 1997, **13**, 2390–2397.
35 V. Pascual-Llorens, A. Serra, P. Mazaira-Couce, M. Escudero-Escribano and P. Sebastián-Pascual, *ChemElectroChem*, 2024, **11**(20), e202400414.
36 Y. Grunder, J. Beane, A. Kolodziej, C. A. Lucas and P. Rodriguez, *Surfaces*, 2019, **2**, 145–158.
37 A. Auer, X. Ding, A. S. Bandarenka and J. Kunze-Liebhäuser, *J. Phys. Chem. C*, 2021, **125**, 5020–5028.
38 P. Sebastián-Pascual and M. Escudero-Escribano, *ACS Energy Lett.*, 2020, **5**, 130–135.
39 F. Valls Mascaró, M. T. M. Koper and M. J. Rost, *Nat. Catal.*, 2024, **7**, 1165–1172.
40 R. Martínez-Hincapié, A. Rodes, V. Climent and J. M. Feliu, *Electrochim. Acta*, 2021, **388**, 138639.
41 S. J. Raaijman, N. Arulmozhi, A. H. M. da Silva and M. T. M. Koper, *J. Electrochem. Soc.*, 2021, **168**, 96510.
42 J. Ustarroz, J. A. Hammons, T. Altantzis, A. Hubin, S. Bals and H. Terryn, *J. Am. Chem. Soc.*, 2013, **135**, 11550–11561.
43 J. Ustarroz, *Curr. Opin. Electrochem.*, 2020, **19**, 144–152.
44 R. M. Arán-Ais, R. Rizo, P. Grosse, G. Algara-Siller, K. Dembélé, M. Plodinec, T. Lunkenbein, S. W. Chee and B. R. Cuenya, *Nat. Commun.*, 2020, **11**, 3489.
45 D. Torres, M. Bernal and J. Ustarroz, *Small Methods*, 2025, **9**, 2401029.
46 K. J. Klaas, E. P. Gallent and M. T. M. Koper, *J. Electroanal. Chem.*, 2013, **699**, 6–9.
47 L. Chico-Mesa, A. Rodes, R. M. Arán-Ais and E. Herrero, *Nat. Commun.*, 2025, **16**, 3349.
48 Q. Qin, T. Li, X. Sun, A. Pei, Y. Jia, H. He, F. Gao, P. Wang, Q. Wu, R. Liu, S. Dai, H. Lin, Q. Zhang, Y. Zhao and G. Chen, *Nano Lett.*, 2024, **24**, 16351–16359.
49 H. Liu, N. Agrawal, A. Ganguly, Y. Chen, J. Lee, J. Yu, W. Huang, M. Mba Wright, M. J. Janik and W. Li, *Energy Environ. Sci.*, 2022, **15**, 4175–4189.
50 N. Hoshi and Y. Hori, *Electrochim. Acta*, 2000, **45**, 4263–4270.
51 C. Hahn, T. Hatsukade, Y.-G. Kim, A. Vailionis, J. H. Baricuatro, D. C. Higgins, S. A. Nitopi, M. P. Soriaga and T. F. Jaramillo, *Proc. Natl. Acad. Sci. U. S. A.*, 2017, **114**, 5918–5923.
52 J. A. Gauthier, J. H. Stenlid, F. Abild-Pedersen, M. Head-Gordon and A. T. Bell, *ACS Energy Lett.*, 2021, **6**, 3252–3260.
53 E. Pérez-Gallent, M. C. Figueiredo, F. Calle-Vallejo and M. T. M. Koper, *Angew. Chem., Int. Ed.*, 2017, **56**, 3621–3624.
54 K.-L. C. Nguyen, J. P. Bruce, A. Yoon, J. J. Navarro, F. Scholten, F. Landwehr, C. Rettenmaier, M. Heyde and B. R. Cuenya, *ACS Energy Lett.*, 2024, **9**, 644–652.